PCCP

ROYAL SOCIETY OF CHEMISTRY

PAPER

View Article Online
View Journal | View Issue

Cite this: *Phys. Chem. Chem. Phys.*, 2025, **27**, 24024

Assigning flavin's difference-FTIR spectral bands in solution: frequency and intensity shifts in flavin's 1-electron and 2-electron reduced states

D. P. Ngan Le, [a] Gary Hastings *[ab] and Samer Gozem *[a]

Flavins are versatile cofactors that undergo different redox, chemical, and/or photophysical transformations depending on the protein they are bound to. A powerful tool available for studying these transformations is Fourier transform infrared (FTIR) difference spectroscopy, where changes in the FTIR absorption bands relate to specific changes in flavin's bonding or interactions with its neighboring environment. While the infrared (IR) spectra of oxidized flavins are well-characterized, fewer computational and experimental studies have focused on characterizing the IR spectra of flavins in their reduced (radical semiquinone or hydroquinone) states. Here, we employ hybrid quantum mechanical/molecular mechanical (QM/MM) models with implicit solvation to compute vibrational frequencies and IR intensities for a model flavin (lumiflavin) in its oxidized, anionic semiquinone, anionic hydroquinone, and neutral hydroquinone states. The water solvent configurations around the flavin are sampled with molecular dynamics for each state. These simulations, applied with semi-empirically determined broadening and frequency-scaling factors, are used to assign the main features of experimental FTIR difference spectra in the diagnostic 1350–1750 cm^{-1} range from a variety of sources. The calculations show distinct, redox-state-dependent frequency shifts, especially for C=O stretching bands and C=N stretching bands, consistent with changing formal bond orders in flavin's pteridine rings upon reduction. These shifts can serve as spectral fingerprints for specific radical and 2-electron reduced forms, which will aid in interpreting these bands in FTIR difference spectroscopy measurements of flavoproteins.

Received 16th June 2025,
Accepted 22nd October 2025

DOI: 10.1039/d5cp02306h

rsc.li/pccp

I. Introduction

Flavins are essential redox-active cofactors involved in various biological processes, including electron transfer, catalysis, and photoactivation.[1–3] Flavin mononucleotide (**FMN**) and flavin adenine dinucleotide (**FAD**) are the most prevalent flavins in biological systems, playing key roles in catalysis (flavoenzymes)[1,4] and mediating response to light (photoreceptors).[5–8] Underpinning flavin's versatility is their ability to exist in multiple redox states, most prominently oxidized, one-electron reduced (semiquinone radical), and two-electron reduced (hydroquinone) states. Each of these states can adopt different protonation forms depending on pH.[9–12]

Fig. 1 shows several physiologically relevant redox and protonation states of flavins, using lumiflavin (**LF**) as a model compound. The oxidized form (**LF**) undergoes one-electron reduction to form semiquinone radicals, which exist in either neutral ($\mathbf{LFH^{\bullet}}$) or anionic ($\mathbf{LF^{\bullet -}}$) states. Further reduction produces the hydroquinone form, which can be neutral ($\mathbf{LFH_2}$) or anionic ($\mathbf{LFH^{-}}$).

Flavin's redox, chemical, or photophysical transformations are often followed using FTIR difference spectroscopy, which is an effective tool for probing such transformations with molecular level specificity. FTIR difference spectroscopy is typically undertaken using spectroelectrochemistry[13–15] or time-resolved (TR), step-scan FTIR difference spectroscopy methods.[16–19] The latter is widely used to study the molecular mechanisms underlying flavoprotein photoreception.[20–90] Spectroelectrochemistry and TR-FTIR experiments generate difference spectra, which highlight vibrational changes between states by subtracting one spectrum from another (Fig. 2).[19] Several of the experimental studies cited above were accompanied by electronic structure calculations, or prompted independent computational studies to interpret the experiments, usually by simulating so-called light-minus-dark FTIR difference spectra.[91–95] Together, theory and experiments can construct an atomic-level picture of molecular events following a redox or photoexcitation event.

The IR spectra of oxidized flavins have been characterized through experimental spectro-electrochemistry and TR-FTIR

[a] *Department of Chemistry, Georgia State University, Atlanta, Georgia 30303, USA. E-mail: ghastings@gsu.edu, sgozem@gsu.edu*
[b] *Department of Physics and Astronomy, Georgia State University, Atlanta, Georgia 30303, USA*

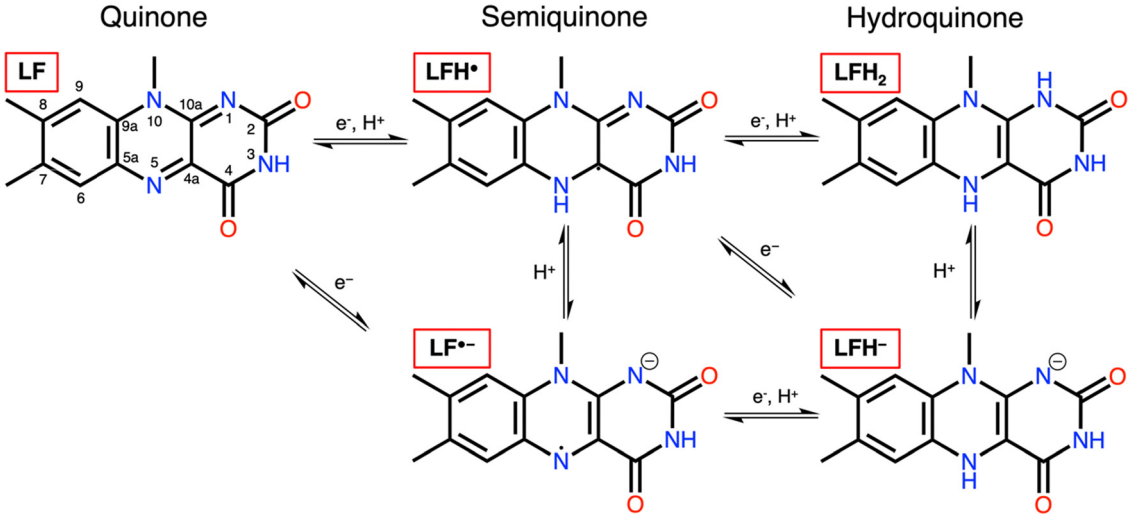

Fig. 1 Five flavin redox and protonation states for lumiflavin (**LF**). The atom numbering is shown for the oxidized quinone structure.

difference spectroscopy experiments cited above, and through steady-state FTIR spectroscopy[97–102] and computational studies.[103–108] We also recently showed that key vibrational frequencies can be reproduced for flavin in aqueous solution using either an implicit polarizable continuum model (PCM) or explicit solvent model.[106,107] The latter often requires adequate sampling of hydrogen bonding interactions with the solvent and treatment of water molecules close to the flavin quantum mechanically. However, simulating relative band intensities remains challenging, particularly for C=C and C=N stretching vibrations. These intensities are sensitive to vibrational coupling that can be influenced by minor frequency shifts of only a few cm^{-1}.[107] As a result, accurate intensity predictions require advanced models that account for both short-range hydrogen bonding and long-range electrostatic interactions.[103,104,107]

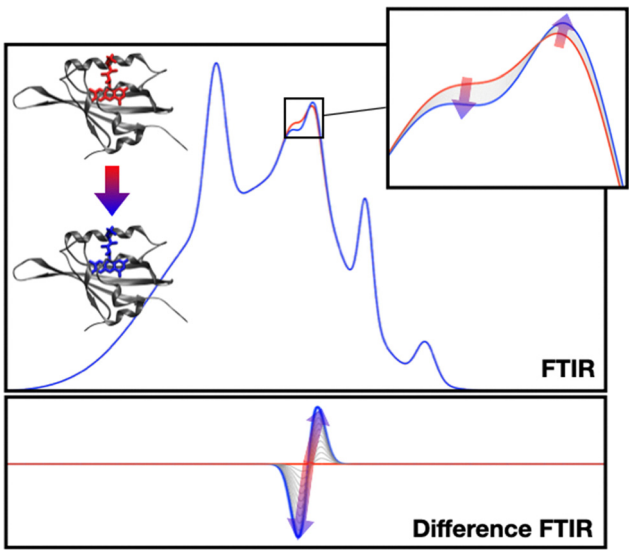

Fig. 2 Top: A schematic representation showing the principles of FTIR difference spectroscopy measurements for a redox change in a flavoprotein. The protein structure is shown for a representative flavoprotein, *Arabidopsis thaliana* LOV2, PDB ID 4eep.[96] The spectrum is just a cartoon and not a real spectrum. The FTIR spectrum of a protein before (red) and after (blue) a redox process are represented in the top panel. The change, shown magnified in the inset, is due to alterations in a few molecular bonds near the site of radical formation within the protein, and is normally very weak compared to the IR signals of the entire protein and solvent. Bottom: FTIR difference spectrum obtained by subtracting the red (initial) from the blue (final) spectrum. The changes due to redox processes are now clear with most of the protein and solvent absorption cancelling out.

In contrast to studies of oxidized flavins, relatively few computational and experimental studies have focused on characterizing the FTIR spectroscopy signals of flavins in their reduced (semiquinone or hydroquinone) states, even though those reduced states are often key intermediates in the mechanisms of flavin-binding photoreceptors and (photo)enzymes. Recently, Huix-Rotllant, Schwinn and Ferré[108] simulated a (**FADH•–FAD**) difference spectrum for cryptochrome using an efficient analytic second derivative and local normal mode analysis that they developed for hybrid quantum mechanical/molecular mechanical (QM/MM) models.[109–113] Furthermore, some of the computational QM/MM protocols developed and applied to simulate light-minus-dark signals in flavoproteins, such as those by Menucci and co-workers[91,92] and Hammes-Schiffer and co-workers,[93] may similarly be applied to simulate reduced-minus-oxidized signals in flavoproteins.

Because even minor deviations in vibrational frequencies or intensities can be amplified in difference spectra, the accurate simulation of difference spectra remains a challenge. In this study, we extend our previously successful computational protocol for simulating the IR spectrum of oxidized flavin[107] to three other redox states: the anionic semiquinone, anionic hydroquinone, and neutral hydroquinone states. We use those calculations to produce FTIR difference spectra, which we compare to spectroelectrochemistry[15] and TR-FTIR experiments,[40] allowing us to identify and characterize major experimental peaks. The neutral semiquinone was not included since we could not find an experimental spectrum for this species. The assignments we suggest provide a reference for interpreting TR-FTIR data in all

flavin-binding systems, which will aid in our understanding of flavin redox (bio)chemistry.

II. Computational methods

Model system selection

Since redox state changes are localized to the flavin's isoalloxazine ring, we use LF as a model system for FTIR spectral simulations instead of **FMN** or **FAD**. This approach reduces the computational cost while retaining the key structural moiety responsible for flavin's redox chemistry. Previous QM/MM vibrational frequency calculations on cryptochrome have shown that the IR spectrum of **FAD** in the 1350–1750 cm^{-1} range is primarily determined by isoalloxazine vibrations, with only minor adenine contributions around 1600 cm^{-1}.[108] Other moieties, such as the diphosphate, ribityl, and ribose groups, exhibit negligible contributions to vibrations in that range. In difference spectra, contributions from the adenine are expected to cancel out for the different redox states. Thus, the **LF** model allows us to isolate essential vibrational features relevant to flavin redox behavior.

In previous work focused on the oxidized state of **LF**, we compared vibrational frequency calculations of gas-phase QM cluster models,[106] QM/PCM models,[106,107] QM/MM models,[107] and QM/MM/PCM[107] models to the experimental FTIR spectra of flavin in aqueous solution.[40,102,105] We found that QM cluster models only reproduced the relative frequencies of the most intense bands appearing in the 1400–1700 cm^{-1} range after accounting for multiple hydrogen-bonding interactions, but could not reproduce the relative intensities of the bands.[106] QM/PCM better reproduced the relative positions and intensities of those bands but introduced an artifact; an additional intense band appeared computationally at 1520 cm^{-1}, although such a band did not exist in the experimental spectrum.[106] In ref. 107, we compared a series of QM/MM protocols for simulating the FTIR spectrum of **LF** in water. The first model, termed **M1**, treated **LF** quantum mechanically and the water solvent molecules all at the MM level of theory. The second protocol, **M2**, expanded the QM region to include water molecules near flavin's hydrophilic pyrimidine ring. The third protocol, **M3**, additionally incorporates long-range electrostatic effects by using a hybrid QM/MM/PCM approach through the ONIOM/PCM-X approach,[114–117] which includes a PCM[118] environment around the entire QM/MM system. This hybrid **M3** approach captures explicit local hydrogen bonding at the QM level, short and medium-range electrostatic interactions at the QM/MM level, and long-range solvation effects *via* implicit PCM. We found that the **M3** protocol gave the best agreement with experimental spectra when adequately sampling the water environment around the flavin using molecular dynamics (MD) simulations.[107] The MD sampling is necessary, since a single snapshot or a few snapshots do not reproduce the experimental spectra well. We found that 100 snapshots is adequate and gave a good agreement with the experimental spectra.[107] These earlier benchmark studies inform the computational approach used here, which will also follow a slightly modified version of protocol **M3**.

MD simulations

For each redox state of **LF**, MD simulations were performed in a cubic water box with a minimum 3 Å distance between the

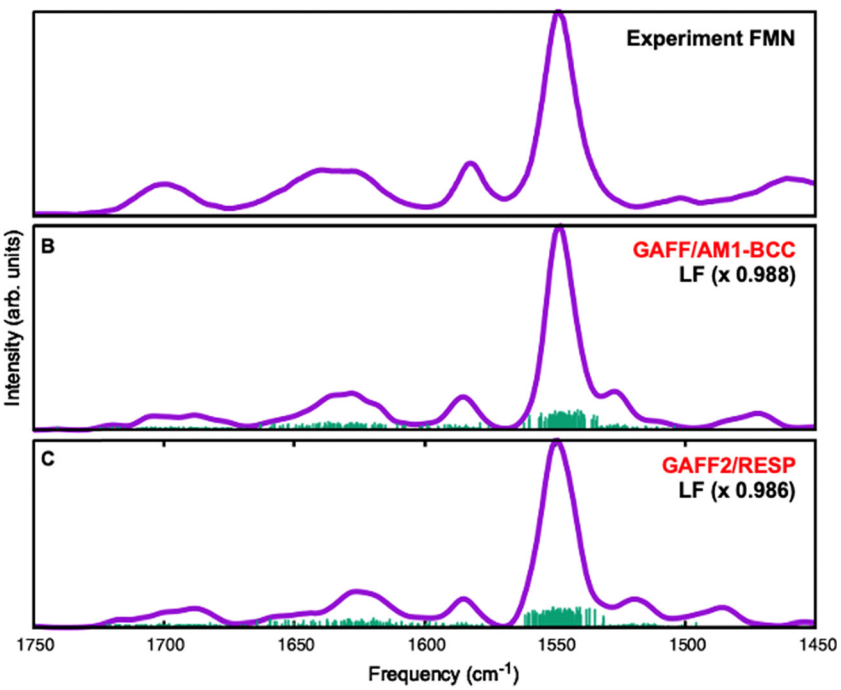

Fig. 3 Comparison between experimental (A) oxidized **FMN**[97] and computed FTIR spectra of LF in two different force field (parameters) and charge methods (B) GAFF/AM1-BCC (from ref. 107) (C) GAFF2/RESP (this work). The computed vibrational lines (green) were convolved with 8 cm^{-1} wide (FWHM) Gaussian functions and summed to give the simulated spectra (purple).

solute atoms and the box edge. This smaller box size minimizes the computational cost of subsequent QM/MM/PCM calculations, which scale unfavorably with the size of the PCM cavity enclosing the full QM/MM system. We previously tested an expanded 12 Å solvent box for oxidized **LF** and found it had minimal impact on the simulated spectrum compared to the smaller solvent box generated at 3 Å from the flavin edge, which is an indication that the smaller periodic solvent box still allows for adequately sampling the water configurations around the **LF**.[107]

Water was modeled using the TIP3P force field,[119] with a sodium ion (Na^+) replacing one water molecule to maintain overall charge neutrality for the anionic semiquinone and hydroquinone states. **LF**'s parameters were derived from GAFF2, with RESP-assigned charges,[120] marking a slight deviation from our previous GAFF[121]/AM1-BCC[122] approach for oxidized **LF** used previously in the **M3** protocol.[107] Since the flavin structure is refined at the QM/MM level of theory, spectra computed using the two parameter sets were very similar (see Fig. 3B and C), suggesting that short-range water orientation around **LF** is not strongly dependent on the charge model. In other words, the small discrepancies from the MM force field, which may not be optimal for charged species,[123] are likely removed by the QM/MM optimization prior to frequency analysis. Related electrostatic potential fitting methods have also been well tested for flavins as part of a different QM/MM protocol, namely, the average protein electrostatic configuration approach for flavoproteins.[123–130]

Hydroquinones ($\mathbf{LFH_2}$ and $\mathbf{LFH^-}$) are known to adopt a bent "butterfly" conformation in their ground state.[131–134] However, the standard GAFF2 protocol incorrectly results in a planar geometry. To address this, we manually adjusted force field assignments, redefining the central nitrogen atoms (N5 and N10) as sp^3 instead of sp^2, yielding the expected bent geometry in MM minimizations. We note that when we use the planar force field, the QM/MM optimizations partially correct the structures by introducing some degree of bending, although this bending is sterically limited by the surrounding (frozen) solvent. This led to some worsening of the agreement between the spectrum simulated with the planar force field and the experimental difference spectrum (see Fig. S1 in the SI document). In contrast, the simulations using the modified (bent) force fields for $\mathbf{LFH_2}$ give more well-defined peaks in IR difference spectra, with their calculated frequencies in better agreement with experiment. Overall, the best combination—GAFF2/RESP for **LF** and GAFF2/RESP with the modified bent force field for $\mathbf{LFH_2}$—led to a small improvement in agreement with experimental spectra (Fig. S1).

The MD simulations began with a 5 ns gradual thermalization from 0 K to 300 K with constant volume and temperature (NVT) ensemble, followed by an equilibration at 1 bar for an additional 5 ns at the constant pressure and temperature (NPT) ensemble. Periodic boundary conditions[135] and particle-mesh Ewald[136,137] were applied, with an electrostatic interaction cutoff set to 5 Å during those steps. Next, we ran an additional 5 ns NPT equilibration where we reduced the cutoff to 4 Å out of an abundance of caution to prevent flavin interacting with itself through the periodic boundary walls. If the average pressure exceeded 3 bar or was smaller than 0.5 bar during the NPT MD, we repeated this equilibration step until the pressure gets closer to 1 bar. Lastly, we carry out an NVT production simulation for 5 ns using the average volume from the NPT equilibration run. MD simulations were conducted using AMBER 20 software package.[138,139]

Quantum mechanics/molecular mechanics (QM/MM) calculations

We selected 100 snapshots from the production phase of the MD simulations for QM/MM geometry optimizations and vibrational frequency calculations. The QM/MM models were set up following the **M3** protocol previously reported for oxidized **LF**.[107] For each redox state, the QM region was defined as lumiflavin plus all water molecules with at least one atom within 3.5 Å of any flavin carbonyl oxygen, identified using VMD.[140] The remaining solvent molecules were treated using the TIP3P MM force field. On average, the number of QM water molecules per snapshot was 10.11 for **LF**, 11.56 for $\mathbf{LF^{\bullet -}}$, 11.75 for $\mathbf{LFH^-}$, and 10.38 for $\mathbf{LFH_2}$; these values were obtained by counting the QM waters in each of the 100 snapshots and calculating the mean for each state.

The QM/MM calculations were carried out using the ONIOM/PCM-X approach.[114–117] Geometry optimizations and harmonic frequency calculations for each snapshot were performed at the B3LYP/6-31+G* level using electrostatic embedding in Gaussian 16.[141] Geometry optimizations were terminated when a maximum RMS gradient of 0.003 atomic units or lower was achieved. We then repeated the calculations for 10 of the 100 **LF** structures using the B3LYP-D3 functional to examine the influence of dispersion interactions on the computed vibrational frequencies.[142]

The reference experimental data used here were obtained in aqueous solution, but some of the experiments were recorded in deuterated solvent (D_2O). When comparing against experimental data in D_2O, we replace the exchangeable protons on flavin with deuterium—specifically, those on N1, N3, and N5 (if protonated for a given redox state). That said, we opted to treat all quantum and molecular mechanical waters as deuterated in this work, regardless of the experimental conditions. This choice is advantageous as it excludes H_2O bending modes that typically appear near 1630 cm^{-1}. While these modes should cancel out in difference spectra between redox states, perfect cancellation would require extensive sampling of water configurations, which is computationally impractical. By deuterating these waters, their bending modes shift to lower frequencies ($\sim$1200 cm^{-1}) and thus appear outside the diagnostic window. Deuteration of the solvent, while maintaining isotope consistency with the experiment for flavin's exchangeable protons, is expected to have a minimal effect on the spectrum in the region 1350–1750 cm^{-1}, as suggested by previous experiments[15] and our calculations reported below.

To complement these QM/MM **M3** simulations, we optimized **LF** in each redox state and computed their vibrational frequencies in an exclusively implicit IEF-PCM solvent

model,[143] providing a secondary reference for comparison with QM/MM-computed difference spectra.

Spectral simulations

Computed vibrational frequencies and intensities were broadened with Gaussian functions (typically, full-width at half-maximum FWHM = 8 cm^{-1} for ONIOM/PCM-X and FWHM = 16 cm^{-1} for IEF-PCM, unless indicated otherwise) and scaled by a constant factor. These FWHMs and scaling factors were chosen empirically to improve agreement with experimental data. Scaling vibrational frequencies is standard practice to account for anharmonicity; the Computational Chemistry Comparison and Benchmark DataBase (CCCBDB)[144] recommends a scaling factor of 0.964 for B3LYP with a double-zeta Pople basis set including diffuse functions, with an uncertainty of ±0.023. A more recent benchmark study suggests a scaling factor of 0.980 ± 0.007 for B3LYP/double-ζ calculations in the mid-IR (1000–2000 cm^{-1}) range.[145] Our previous benchmarks indicated 0.988 as optimal for oxidized **LF**.[106,107]

The reason for using different FWHM values for PCM and **M3** calculations is because, for ONIOM/PCM-X, we convolve spectra from 100 individual calculations (each with slightly different solvent configurations), which naturally introduces some statistical broadening. Therefore, a smaller FWHM (8 cm^{-1}) suffices to reproduce experimental line widths. In contrast, for IEF-PCM, only a single calculation is performed for each model, so we use a larger FWHM (16 cm^{-1}) to approximately capture broadening that would arise from ensemble averaging.

Here, we apply tailored scaling factors (ranging from 0.965–1.01) for each redox state to maximize agreement with experimental data while remaining close to the CCCBDB uncertainty range. Once the spectra for the oxidized and reduced state are broadened and scaled, the oxidized spectrum (**LF**) was subtracted from the reduced state spectra to simulate IR difference spectra.

Vibrational mode assignment

Vibrational modes were characterized using vibrational energy distribution analysis (VEDA) for the IEF-PCM computed frequencies.[146] VEDA employs internal coordinates optimized to represent theoretical normal modes, to help quantify the contribution of molecular movements associated with specific vibrational frequencies. This process involves decomposing vibrational normal modes into contributions from stretching, bending, torsional, and out-of-plane motions.

III Results and discussion

Fig. 4–7 present the computed IR difference spectra for deuterated [$\mathbf{LFD_2}$–**LF**], protonated [$\mathbf{LFH_2}$–**LF**], [$\mathbf{LFH^-}$–**LF**], and [$\mathbf{LF^{\bullet -}}$–**LF**], respectively. The computed spectra are compared to the corresponding experimental spectra of [$\mathbf{FADD_2}$–**FAD**] in D_2O, [$\mathbf{FADH_2}$–**FAD**] in H_2O, [**FMNH**$^-$–**FMN**] in H_2O, and

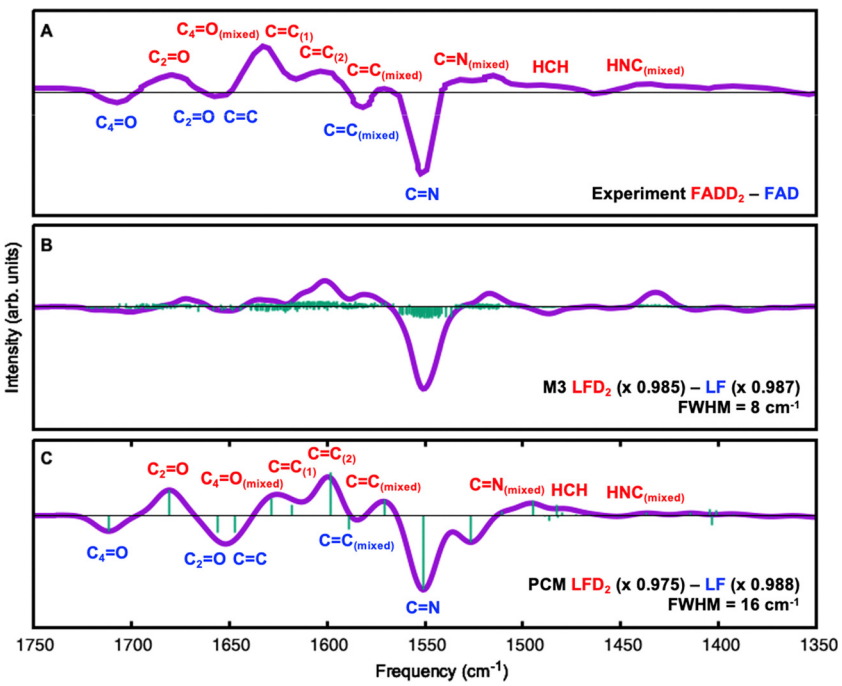

Fig. 4 Comparison between experimental (A) $\mathbf{FADD_2}$–**FAD**[15] in D_2O and computational FTIR difference spectra of deuterated $\mathbf{LFD_2}$–**LF** using (B) protocol **M3**, and (C) IEF-PCM. The horizontal black line within each panel helps distinguish positive from negative peaks. The green impulse lines indicate computed frequencies and intensities and the purple plots in panels B and C are generated by adding Gaussian broadening functions to each transition (8 cm^{-1} FWHM in panel B and 16 cm^{-1} FWHM in panel C). The band assignments, based on QM/PCM VEDA calculations, are indicated in red font for $\mathbf{LFD_2}$ and blue font for deuterated **LF**. The normal modes corresponding to negative and positive bands in panel C are shown in Fig. S3 and S5, respectively, while the percentage contributions of specific modes used to assign the bands are provided in Tables S2 and S4.

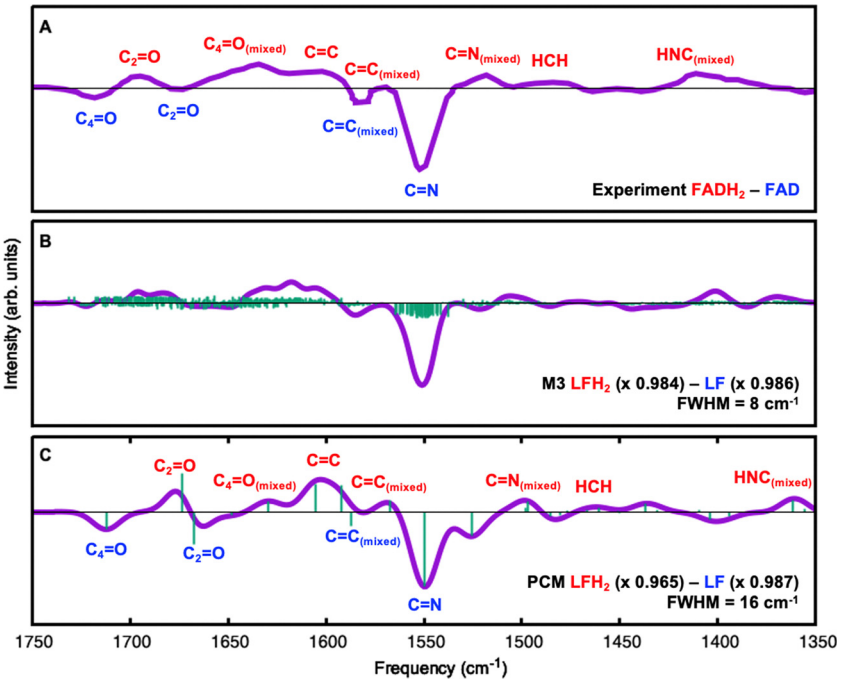

Fig. 5 Comparison between experimental (A) **$FADH_2$–FAD**[15] in H_2O and computational FTIR difference spectra of **LFH_2–LF** redox transition using (B) protocol **M3**, and (C) IEF-PCM. Only hydrogen atoms in water molecules were replaced with deuterium. The horizontal black line within each panel helps distinguish positive from negative peaks. The green impulse lines indicate computed frequencies and intensities and the purple plots in panels B and C are generated by adding Gaussian broadening functions to each transition (8 cm^{-1} FWHM in panel B and 16 cm^{-1} FWHM in panel C). The band assignments, based on QM/PCM VEDA calculations, are indicated in red font for **LFH_2** and blue font for protonated **LF**. The normal modes corresponding to negative and positive bands in panel C are shown in Fig. S2 and S4, respectively, while the percentage contributions of specific modes used to assign the bands are provided in Tables S1 and S3.

[**$FMN^{\bullet-}$–FMN**] in H_2O. In each of the four figures, we present the experimental difference spectra at the top, **M3**-calculated spectra in the middle, and IEF-PCM-calculated spectra at the bottom. The positive bands correspond to the reduced states (**LFD_2**, **LFH_2**, **LFH^-**, or **$LF^{\bullet-}$**), while negative bands represent the oxidized **LF** state.

Overall, the computations reproduce well the frequencies of the main spectral features observed experimentally, though intensity mismatches remain. Before proceeding with comparing the computed and experimental spectra, it is useful to discuss sources of errors and uncertainties in comparing computed vibrational simulations and experiments. As discussed in the Introduction section, difference spectra emphasize spectral changes rather than absolute IR intensities, making them sensitive to computational parameters such as broadening and even small frequency and intensity shifts. Therefore, the same level of agreement between calculations and experiments as obtained, for instance, when simulating a steady-state FTIR spectra (*e.g.*, Fig. 3) is not expected. Accurate simulation of difference spectra also requires that the electronic structure calculations treat the different redox states on an equal footing so that systematic errors cancel out. However, this is not always guaranteed. While B3LYP has been shown to provide reasonable harmonic frequencies for molecular radicals,[147,148] systematic errors may vary between radical semiquinones and closed-shell oxidized **LF** species.[149] The empirically determined scaling factors mitigate such errors but may not fully eliminate them. Additionally, as discussed in the Materials and methods section, the hydroquinone species exhibit non-planar distortions at the central ring, with the extent of bending dependent on the electronic structure method used.[150] This non-planarity may introduce an additional error for the difference spectra between the (non-planar) hydroquinone and (planar) quinone states.

B3LYP does not include a proper accounting of dispersion corrections, which may be relevant to describing the hydrogen-bonding interactions between the QM-treated waters and **LF**. Therefore, we reran the **M3** protocol for 10 **LF** snapshots using B3LYP-D3. The dispersion correction resulted in an overall modest upfield shift relative to the original B3LYP results, with average errors of 4.3, 5.8, 2.2, and 2.5 cm^{-1} for the C_4═O, C_2═O, C═C, and C═N stretching modes, respectively. (Table S7). Since this change is systematic, we expect that the use of dispersion corrections will only lead to a modest change in the overall simulated spectrum.

A third source of error arises from comparing **LF** QM/MM calculations to experimental spectra of **FMN** and **FAD** in complex media. Experimental spectro-electrochemistry and TR-FTIR experiments rely on signal subtraction to isolate small vibrational changes associated with redox transitions, often requiring the removal of large solvent and protein signals. As shown in Fig. 2, the full FTIR spectra before (red) and after (blue) a redox or photochemical event differ only slightly. These subtle changes become clear only after generating a FTIR

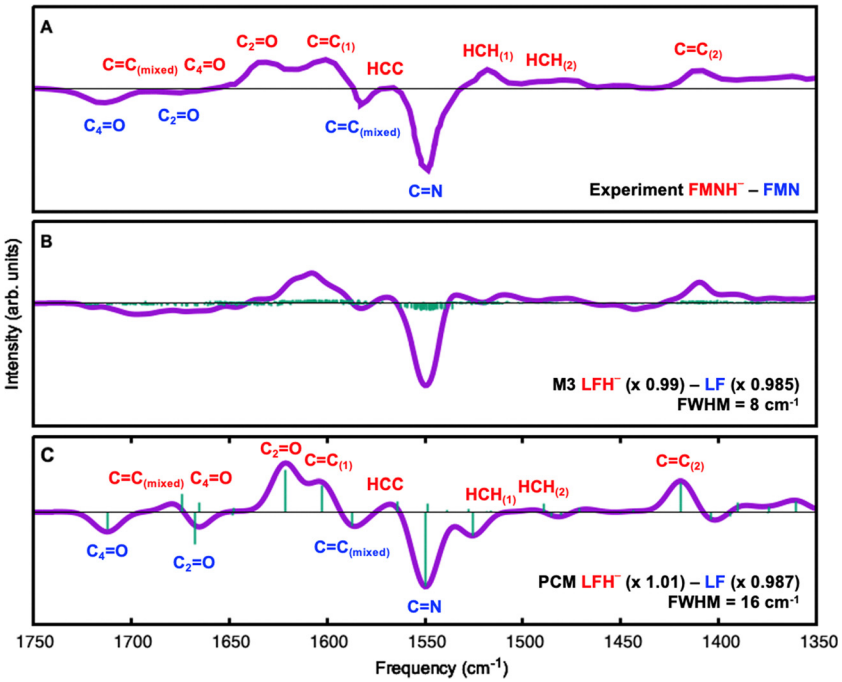

Fig. 6 Comparison between experimental (A) **FMNH$^-$–FMN**[40] in H_2O and computational FTIR difference spectra of **LFH$^-$–LF** redox transition using (B) protocol **M3**, and (C) IEF-PCM. Only hydrogen atoms in water molecules were replaced with deuterium. The horizontal black line within each panel helps distinguish positive from negative peaks. The green impulse lines indicate computed frequencies and intensities and the purple plots in panels B and C are generated by adding Gaussian broadening functions to each transition (8 cm^{-1} FWHM in panel B and 16 cm^{-1} FWHM in panel C). The band assignments, based on QM/PCM VEDA calculations, are indicated in red font for **LFH$^-$** and blue font for protonated **LF**. The normal modes corresponding to negative and positive bands in panel C are shown in Fig. S2 and S6, respectively, while the percentage contributions of specific modes used to assign the bands are provided in Tables S1 and S5.

difference spectrum (Fig. 2, bottom panel), where subtraction isolates redox-associated spectral features. However, the process of generating a difference spectrum by subtracting two nearly identical spectra can amplify measurement noise and small baseline variations, making the detection of subtle redox-associated features more challenging compared to direct FTIR measurements of samples. Achieving complete redox conversion is another experimental challenge; reaction kinetics and equilibrium conditions often result in mixed states, further complicating spectral interpretation. For example, the semiquinone state is unstable in solution, forming only transiently, while additional side reactions with the solvent may introduce secondary species. Experimental conditions, such as the presence of buffer components (*e.g.*, EDTA in ref. 40) that may interact differently with the reduced and oxidized flavin states, can alter the observed spectra. In contrast, computational models assume complete redox transitions and pure states, which may not fully represent the experimental complexities reflected in FTIR difference spectra.

The use of a few empirical parameters (*e.g.*, scaling factors and broadening) in these simulations means that the computational models may not yet be suitable for predictive simulations of FTIR difference spectra in the absence of an experimental reference. This is especially true for spectra of states with a different charge, since the scaling factor for the negatively charged **LF$^{\bullet-}$** and **LFH$^-$** states are significantly different (0.99–1.01) than the scaling factor for the neutral **LF** state (0.985–0.988). However, we note that for the **M3** protocol, the scaling factor used for the neutral **LFH_2** state (0.984–0.985) is comparable to the **LF** one. Despite these limitations in absolute frequency prediction, calculated difference spectra are particularly valuable for identifying systematic trends across redox states. For example, the computed bands of oxidized, semireduced, and fully reduced flavins (or quinones) often shift in frequency or change in intensity in a consistent and recognizable pattern as the oxidation state changes. Such trends, even if not quantitatively exact, can provide critical guidance for interpreting experimental FTIR difference spectra and for assigning bands to specific redox transitions. Thus, while empirical adjustment is required for direct comparison with experiment, the computational approach remains a powerful tool for revealing qualitative trends and mechanistic insights.

To assign the peaks to specific vibrations, we visualized the normal modes and characterized them using VEDA on the IEF-PCM calculations. We use the singular IEF-PCM calculation since it is easier to carry out the analysis compared to the **M3** protocol which involves 100 QM/MM vibrational frequency calculations. The difference spectra in Fig. 4–7 indicate that the IEF-PCM model on its own introduces artifacts (*e.g.*, a spurious negative band near 1520 cm^{-1}) and does not capture solvent-induced broadening. In contrast, the **M3** (QM/MM/PCM) protocol recovers both realistic line widths and experimentally observed band shapes, while still being consistent with frequency assignments made from the simpler QM/PCM model. Thus, while QM/PCM is suitable for assignments, the **M3** protocol provides the more accurate description of experimental IR difference spectra.

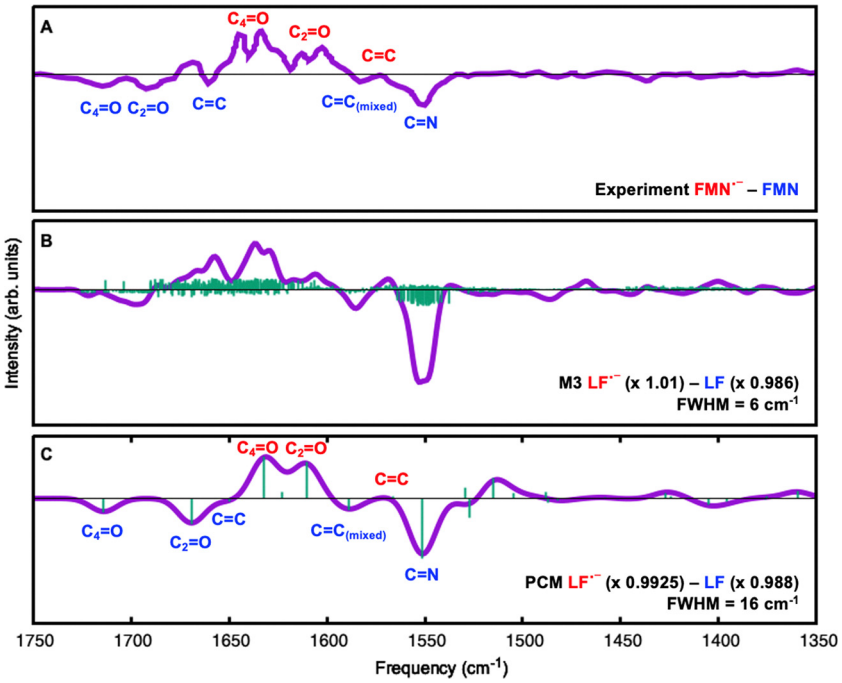

Fig. 7 Comparison between experimental (A) **FMN**$^{\bullet-}$**–FMN**[40] in H_2O and computational FTIR difference spectra of **LF**$^{\bullet-}$**–LF** redox transition using (B) protocol **M3**, and (C) IEF-PCM. Only hydrogen atoms in water molecules were replaced with deuterium. The horizontal black line within each panel helps distinguish positive from negative peaks. The green impulse lines indicate computed frequencies and intensities and the purple plots in panels B and C are generated by adding Gaussian broadening functions to each transition (6 cm^{-1} FWHM in panel B and 16 cm^{-1} FWHM in panel C). The band assignments, based on QM/PCM VEDA calculations, are indicated in red font for **LF**$^{\bullet-}$ and blue font for protonated **LF**. The normal modes corresponding to negative and positive bands in panel C are shown in Fig. S2 and S7, respectively, while the percentage contributions of specific modes used to assign the bands are provided in Tables S1 and S6.

In Fig. S2–S7, the atomic motions within the normal modes are shown for protonated **LF**, deuterated **LF**, protonated $\mathbf{LFH_2}$, deuterated $\mathbf{LFD_2}$, protonated $\mathbf{LFH^-}$ and protonated $\mathbf{LF^{\bullet-}}$, respectively. Displacement vectors illustrate the atomic motions while the labels identify the dominant molecular group vibrations assigned using VEDA. Further details about the decomposition of each normal mode to internal coordinates are presented in Tables S1–S6 in the SI. In Tables S1–S6, the percentage values indicate each molecular groups contribution to a given vibrational mode frequency: positive values denote direct contributions, while negative values reflect out-of-phase contributions.

A vibrational mode is considered dominant when it is the only mode listed by VEDA, or when its contribution exceeds 50%, indicating minimal mixing with other modes. For example, the C_4═O stretching mode in $\mathbf{LFH_2}$ (1629 cm^{-1}, 23% contribution, Table S3) is classified as mixed in Fig. 5C due to its contribution being below the 50% threshold. In contrast, the C═C stretching mode of **LF** (1650 cm^{-1}, 55% contribution, Table S1) is dominant, with smaller overlap with other modes, and so is labeled just as C═C.

PCM introduces a pronounced negative band near 1520 cm^{-1} (*e.g.*, compare panel C in Fig. 4–6 to panel A in the same figures), previously identified as an artifact caused by coupling of vibrational modes when using PCM with a high dielectric constant.[106,107] This artifact is mitigated in the **M3** protocol (see panel B in Fig. 4–6).

Several spectral features are consistent across all redox states (Fig. 4–7). The most prominent bands include C═O stretching vibrations at the highest frequencies (~1650–1750 cm^{-1}), with C═C and C═N stretching and bending vibrations at lower frequencies. Both the PCM and **M3** models successfully capture these frequency trends, though the PCM model often yields spectra with better-defined C═O peaks that are more in line with experiments. The **M3** model predicts broader and lower intensity C═O bands. As noted in previous studies, intensity predictions are challenging even for the oxidized form (**LF**),[107] and this issue is shown to persist across the other redox states here. Conversely, in the lower frequency regions, the **M3** calculated spectra generally align better with experimental spectral data; PCM calculated spectral data can either overestimate or underestimate bending mode band intensities, while **M3** models provides spectral profiles more consistent with experiments. Together, the **M3** and PCM models offer a complementary approach to spectral band analysis in this work: the **M3** model aids in assigning lower-frequency bands alongside the PCM model, while the PCM model helps better discern higher-frequency (especially C═O) bands.

While general trends are similar across redox states, some key differences emerge, which we discuss below in light of the spectral band assignments made based on our computations.

C═O stretching modes

Table 1 summarizes some of the shifts observed for a few key C═O, C═N, and C═C stretching modes upon the reduction of the flavin cofactor. The C_2═O band of **LF** upshifts 4/25 cm^{-1}

Table 1 IR spectral shifts (in cm^{-1}) of five vibrational bands upon reduction of the oxidized flavin species computed at the QM/PCM level of theory. Shifts are shown for both radical (semiquinone) and 2e-reduced (hydroquinone) forms. Negative values indicate downshifts (to lower frequency), and positive values indicate upshifts (to higher frequency) relative to the oxidized state. Band assignments are based on QM/PCM VEDA calculations

	C_4═O	C_2═O	C═C	C═$C_{(mixed)}$	C═N
Deuterated **LF** → **LFD_2**	−83	25	−29/−49	−18	−56
Protonated **LF** → **LFH_2**	−85	4	—	−22	−54
Protonated **LF** → **LFH^-**	−49	−48	—	85	—
Protonated **LF** → **$LF^{\bullet-}$**	−82	−59	−84	—	—

upon **LFH_2**/**LFD_2** formation, respectively. The C_4═O band of **LF** downshifts over 80 cm^{-1} upon **LFH_2** formation independent of deuteration/protonation. This reverses the relative ordering of the C_4═O and C_2═O mode frequencies for the reduced form compared to the oxidized form. This redox-induced reorganization of modes likely results from conjugation between C_4═O and the adjacent C═C bond, leading to mode mixing (see Tables S3 and S4), while protonation of the N1 atom reduces the conjugation of C_2═O with other double bonds, resulting in the small upshift in its frequency.

In the case of the anionic hydroquinone, we see a very different trend, where both the C_4═O and C_2═O downshift ~50 cm^{-1} upon **LFH^-** formation. Somewhat similarly, for the anionic semiquinone state (**LFH^-**, Fig. 7), the C_4═O/C_2═O mode downshifts ~80/60 cm^{-1}, respectively. The difference spectrum of **$FMN^{\bullet-}$** in Fig. 7 is also quite interesting; the bands appear to be somewhat narrower and there is an apparent splitting of the bands associated with the carbonyl stretching vibrations. Fig. 7B demonstrates that the **M3** model can reproduce this splitting when a reduced convolution factor is used (FWHM of 6 cm^{-1} rather than 8 cm^{-1}). The PCM model does not exhibit the same C═O band splitting (Fig. 7C). This latter observation indicates that the C═O peak splitting may originate from solvent hydrogen bonding configurations rather than from the electronic structure of flavin. Both **M3** and PCM models, however, predict C═O band positions (frequencies) consistent with the experimental spectra.

We also note that bands due to C═O stretching modes of **$LF^{\bullet-}$** are more intense than that observed for the other reduced states. Note that intensity here is discussed relative to the oxidized form, which is constant reference state in all spectra. This (relative) high intensity of the C═O stretching modes of **$LF^{\bullet-}$** is observed also in the experimental spectra.

C═N and C═C stretching modes

In all difference spectra (Fig. 4–7), the pronounced negative C═N band of **LF** near 1550 cm^{-1} becomes significantly weaker upon flavin reduction. In other words, there is no intense, positive band in the difference spectra corresponding to a pure C═N stretching vibration in any of the reduced states. This is consistent with the change in electronic structure of flavin upon reduction where the formal C═N double bonds are converted to single bonds (see Fig. 1).

Multiple (positive) C═C bands appear in each of the FTIR difference spectra, and those bands are calculated to have mixed character. Due to the number of these mixed C═C bands and their relatively low intensity, they may be difficult to ascertain experimentally and are of less diagnostic utility. However, we note the presence of a C═C band appearing at an unusually low frequency at around 1420 cm^{-1} for **LFH^-** (Fig. 6C). The low frequency of this mode may be associated with bending of the flavin at the central ring and coupling to HNC bending modes appearing in the other hydroquinone states (Fig. 4 and 5) around the same frequency. While VEDA does not identify a strong HNC contribution in the case of **LFH^-**, it can be seen visually in Fig. S6 for this mode.

IV. Conclusions and future directions

We extended our previous work on assigning bands in FTIR spectra of oxidized flavin to other flavin redox forms. Specifically, we applied the hybrid QM/MM/PCM approach, following a protocol (**M3**) that previously was successful in reproducing the FTIR absorption spectrum of oxidized flavin. The **M3** simulations are compared to a simple QM/PCM model where the solvent is treated only as a dielectric, and against experimental spectroelectrochemistry and step-scan FTIR difference spectra for flavin in three redox states. While empirical parameters—such as frequency scaling and broadening factors---are necessary, the **M3** model effectively captures the general features of the of the FTIR difference spectra and reduces artifactual contributions that arise when using the PCM model alone, such as the negative band near 1520 cm^{-1}. The scaling factors used for the **M3** protocol were in the range of 0.984–0.987 for neutral redox states of flavin and 0.990–1.010 for anionic redox states. For PCM, a wider range of scaling factors were needed to obtain reasonable agreement with experiment: 0.965–0.988 for the neutral redox states and 0.9925–1.010 for the anionic states.

For both the **M3** and QM/PCM models, discrepancies in predicted intensities compared to the experimental spectra highlight the need for further benchmarking and methodological refinements, including improvements in the quantum chemical level of theory, enhancements in the QM/MM model, and the incorporation of anharmonic corrections. Nonetheless, the PCM and **M3** calculations presented here are of sufficient quality for assigning and interpreting bands in the experimental difference spectra. The relatively simple QM/PCM approach alone was useful for assigning most of the experimental bands, but the QM/MM/PCM **M3** protocol resulted in several improvements by better capturing frequency shifts and solvent broadening effects. Importantly, of the two methods tested (PCM and **M3**), only the latter can potentially be applied for simulating FTIR difference spectra associated with flavins in proteins. Therefore, the simulated spectra and band assignments reported here can serve as a reference for future QM/MM FTIR calculations, and/or for TR-FTIR and spectroelectrochemistry experiments of flavin-mediated biological redox reactions.

Conflicts of interest

There are no conflicts of interest to declare.

Data availability

The data supporting this article have been included as part of the supplementary information (SI). The supplementary information includes optimized coordinates of lumiflavin in different redox states computed using the IEF-PCM solvation model, figures representing normal modes of vibrational bands discussed in the manuscript, tables of computed vibrational frequencies and VEDA analysis, simulated difference IR spectra obtained with planar and bent force fields, and mean signed errors between B3LYP and B3LYP-D3 frequency calculations. See DOI: **https://doi.org/10.1039/d5cp02306h**.

Acknowledgements

This material is based upon work supported by the National Science Foundation (NSF) under Grant CHE-2047667 (S. G.). D. P. N. L. acknowledges a fellowship from the Molecular Basis of Disease Program at Georgia State University. This work used Expanse at SDSC through allocation CHE180027 from the Advanced Cyberinfrastructure Coordination Ecosystem: Services and Support (ACCESS) program, which is supported by National Science Foundation grants #2138259, #2138286, #2138307, #2137603, and #2138296. We also acknowledge the use of Advanced Research Computing Technology and Innovation Core (ARCTIC) resources at Georgia State University's Research Solutions, made available by the NSF Major Research Instrumentation (MRI) grant number CNS-1920024.

References

1 S. O. Mansoorabadi, C. J. Thibodeaux and H.-W. Liu, The Diverse Roles of Flavin CoenzymesNature's Most Versatile Thespians, *J. Org. Chem.*, 2007, **72**(17), 6329–6342.
2 V. Joosten and W. J. H. van Berkel, Flavoenzymes, *Curr. Opin. Chem. Biol.*, 2007, **11**(2), 195–202.
3 E. Romero, J. R. Gomez Castellanos, G. Gadda, M. W. Fraaije and A. Mattevi, Same Substrate, Many Reactions: Oxygen Activation in Flavoenzymes, *Chem. Rev.*, 2018, **118**(4), 1742–1769.
4 C. T. Walsh and T. A. Wencewicz, Flavoenzymes: versatile catalysts in biosynthetic pathways, *Nat. Prod. Rep.*, 2013, **30**(1), 175–200.
5 J. M. Christie, J. Gawthorne, G. Young, N. J. Fraser and A. J. Roe, LOV to BLUF: Flavoprotein Contributions to the Optogenetic Toolkit, *Mol. Plant*, 2012, **5**(3), 533–544.
6 A. Losi and W. Gartner, The evolution of flavin-binding photoreceptors: an ancient chromophore serving trendy blue-light sensors, *Annu. Rev. Plant Biol.*, 2012, **63**, 49–72.
7 A. Losi, K. H. Gardner and A. Moglich, Blue-Light Receptors for Optogenetics, *Chem. Rev.*, 2018, **118**(21), 10659–10709.
8 K. S. Conrad, C. C. Manahan and B. R. Crane, Photochemistry of flavoprotein light sensors, *Nat. Chem. Biol.*, 2014, **10**(10), 801–809.
9 A. Albert, Quantitative studies of the avidity of naturally occurring substances for trace metals. III. Pteridines, riboflavin and purines, *Biochem. J.*, 1953, **54**(4), 646–654.
10 R. D. Draper and L. L. Ingraham, A potentiometric study of the flavin semiquinone equilibrium, *Arch. Biochem. Biophys.*, 1968, **125**(3), 802–808.
11 Y. Zheng, P. R. Carey and B. A. Palfey, Raman spectrum of fully reduced flavin, *J. Raman Spectrosc.*, 2004, **35**(7), 521–524.
12 D. Su, M. P. Kabir, Y. Orozco-Gonzalez, S. Gozem and G. Gadda, Fluorescence Properties of Flavin Semiquinone Radicals in Nitronate Monooxygenase, *ChemBioChem*, 2019, **20**(13), 1646–1652.
13 Y. El Khoury, L. J. G. W. Van Wilderen and J. Bredenbeck, Ultrafast 2D-IR spectroelectrochemistry of flavin mononucleotide, *J. Chem. Phys.*, 2015, **142**(21), 212416.
14 G. Noll, E. Kozma, R. Grandori, J. Carey, T. Schodl, G. Hauska and J. Daub, Spectroelectrochemical investigation of a flavoprotein with a flavin-modified gold electrode, *Langmuir*, 2006, **22**(5), 2378–2383.
15 G. Wille, M. Ritter, R. Friedemann, W. Mäntele and G. Hübner, Redox-Triggered FTIR Difference Spectra of FAD in Aqueous Solution and Bound to Flavoproteins, *Biochemistry*, 2003, **42**(50), 14814–14821.
16 C. Kötting and K. Gerwert, Proteins in action monitored by time-resolved FTIR spectroscopy, *ChemPhysChem*, 2005, **6**(5), 881–888.
17 M. L. Groot, L. J. van Wilderen and M. Di Donato, Time-resolved methods in biophysics. 5. Femtosecond time-resolved and dispersed infrared spectroscopy on proteins, *Photochem. Photobiol. Sci.*, 2007, **6**(5), 501–507.
18 J. T. Kennis and M.-L. Groot, Ultrafast spectroscopy of biological photoreceptors, *Curr. Opin. Struct. Biol.*, 2007, **17**(5), 623–630.
19 V. A. Lorenz-Fonfria, Infrared Difference Spectroscopy of Proteins: From Bands to Bonds, *Chem. Rev.*, 2020, **120**(7), 3466–3576.
20 T. E. Swartz, P. J. Wenzel, S. B. Corchnoy, W. R. Briggs and R. A. Bogomolni, Vibration spectroscopy reveals light-induced chromophore and protein structural changes in the LOV2 domain of the plant blue-light receptor phototropin 1, *Biochemistry*, 2002, **41**(23), 7183–7189.
21 T. Iwata, S. Tokutomi and H. Kandori, Photoreaction of the cysteine S–H group in the LOV2 domain of Adiantum phytochrome3, *J. Am. Chem. Soc.*, 2002, **124**(40), 11840–11841.
22 K. Ataka, P. Hegemann and J. Heberle, Vibrational spectroscopy of an algal Phot-LOV1 domain probes the molecular changes associated with blue-light reception, *Biophys. J.*, 2003, **84**(1), 466–474.
23 T. Iwata, D. Nozaki, S. Tokutomi, T. Kagawa, M. Wada and H. Kandori, Light-induced structural changes in the LOV2 domain of Adiantum phytochrome3 studied by low-temperature FTIR and UV-visible spectroscopy, *Biochemistry*, 2003, **42**(27), 8183–8191.

24 D. Nozaki, T. Iwata, T. Ishikawa, T. Todo, S. Tokutomi and H. Kandori, Role of Gln1029 in the photoactivation processes of the LOV2 domain in adiantum phytochrome3, *Biochemistry*, 2004, **43**(26), 8373–8379.

25 T. Bednarz, A. Losi, W. Gärtner, P. Hegemann and J. Heberle, Functional variations among LOV domains as revealed by FT-IR difference spectroscopy, *Photochem. Photobiol. Sci.*, 2004, **3**(6), 575–579.

26 D. Nozaki, T. Iwata, S. Tokutomi and H. Kandori, Water structural changes in the activation process of the LOV2 domain of Adiantum phytochrome3, *J. Mol. Struct.*, 2005, **735**, 259–265.

27 Y. Sato, T. Iwata, S. Tokutomi and H. Kandori, Reactive cysteine is protonated in the triplet excited state of the LOV2 domain in Adiantum phytochrome3, *J. Am. Chem. Soc.*, 2005, **127**(4), 1088–1089.

28 T. Iwata, D. Nozaki, S. Tokutomi and H. Kandori, Comparative investigation of the LOV1 and LOV2 domains in Adiantum phytochrome3, *Biochemistry*, 2005, **44**(20), 7427–7434.

29 D. Nozaki, T. Iwata, S. Tokutomi and H. Kandori, Unique temperature dependence in the adduct formation between FMN and cysteine SH group in the LOV2 domain of Adiantum phytochrome3, *Chem. Phys. Lett.*, 2005, **410**(1–3), 59–63.

30 T. Iwata, D. Nozaki, Y. Sato, K. Sato, Y. Nishina, K. Shiga, S. Tokutomi and H. Kandori, Identification of the C=O stretching vibrations of FMN and peptide backbone by 13C-labeling of the LOV2 domain of Adiantum phytochrome3, *Biochemistry*, 2006, **45**(51), 15384–15391.

31 T. Iwata, A. Yamamoto, S. Tokutomi and H. Kandori, Hydration and temperature similarly affect light-induced protein structural changes in the chromophoric domain of phototropin, *Biochemistry*, 2007, **46**(23), 7016–7021.

32 T. Majerus, T. Kottke, W. Laan, K. Hellingwerf and J. Heberle, Time-Resolved FT-IR Spectroscopy Traces Signal Relay within the Blue-Light Receptor AppA, *ChemPhysChem*, 2007, **8**(12), 1787–1789.

33 Y. Sato, M. Nabeno, T. Iwata, S. Tokutomi, M. Sakurai and H. Kandori, Heterogeneous Environment of the S–H Group of Cys966 near the Flavin Chromophore in the LOV2 Domain of Adiantum Neochrome1, *Biochemistry*, 2007, **46**(36), 10258–10265.

34 A. Pfeifer, T. Majerus, K. Zikihara, D. Matsuoka, S. Tokutomi, J. Heberle and T. Kottke, Time-resolved Fourier transform infrared study on photoadduct formation and secondary structural changes within the phototropin LOV domain, *Biophys. J.*, 2009, **96**(4), 1462–1470.

35 A. Yamamoto, T. Iwata, Y. Sato, D. Matsuoka, S. Tokutomi and H. Kandori, Light signal transduction pathway from flavin chromophore to the Jα helix of Arabidopsis phototropin1, *Biophys. J.*, 2009, **96**(7), 2771–2778.

36 M. T. Alexandre, R. van Grondelle, K. J. Hellingwerf and J. T. Kennis, Conformational heterogeneity and propagation of structural changes in the LOV2/Jα domain from Avena sativa phototropin 1 as recorded by temperature-dependent FTIR spectroscopy, *Biophys. J.*, 2009, **97**(1), 238–247.

37 T. Koyama, T. Iwata, A. Yamamoto, Y. Sato, D. Matsuoka, S. Tokutomi and H. Kandori, Different role of the Jα helix in the light-induced activation of the LOV2 domains in various phototropins, *Biochemistry*, 2009, **48**(32), 7621–7628.

38 A. Pfeifer, T. Mathes, Y. Lu, P. Hegemann and T. Kottke, Blue light induces global and localized conformational changes in the kinase domain of full-length phototropin, *Biochemistry*, 2010, **49**(5), 1024–1032.

39 M. T. Alexandre, E. B. Purcell, R. van Grondelle, B. Robert, J. T. Kennis and S. Crosson, Electronic and protein structural dynamics of a photosensory histidine kinase, *Biochemistry*, 2010, **49**(23), 4752–4759.

40 C. Thöing, A. Pfeifer, S. Kakorin and T. Kottke, Protonated triplet-excited flavin resolved by step-scan FTIR spectroscopy: implications for photosensory LOV domains, *Phys. Chem. Chem. Phys.*, 2013, **15**(16), 5916–5926.

41 E. Herman, M. Sachse, P. G. Kroth and T. Kottke, Blue-light-induced unfolding of the Jalpha helix allows for the dimerization of aureochrome-LOV from the diatom Phaeodactylum tricornutum, *Biochemistry*, 2013, **52**(18), 3094–3101.

42 W. Laan, M. A. van der Horst, I. H. van Stokkum and K. J. Hellingwerf, Initial characterization of the primary photochemistry of AppA, a blue-light-using flavin adenine dinucleotide-domain containing transcriptional antirepressor protein from Rhodobacter sphaeroides: a key role for reversible intramolecular proton transfer from the flavin adenine dinucleotide chromophore to a conserved tyrosine?, *Photochem. Photobiol.*, 2003, **78**(3), 290–297.

43 S. Masuda, K. Hasegawa, A. Ishii and T.-A. Ono, Light-induced structural changes in a putative blue-light receptor with a novel FAD binding fold sensor of blue-light using FAD (BLUF); Slr1694 of Synechocystis sp. PCC6803, *Biochemistry*, 2004, **43**(18), 5304–5313.

44 K. Hasegawa, S. Masuda and T. A. Ono, Structural intermediate in the photocycle of a BLUF (sensor of blue light using FAD) protein Slr1694 in a Cyanobacterium Synechocystis sp. PCC6803, *Biochemistry*, 2004, **43**(47), 14979–14986.

45 K. Hasegawa, S. Masuda and T.-A. Ono, Spectroscopic analysis of the dark relaxation process of a photocycle in a sensor of blue light using FAD (BLUF) protein Slr1694 of the cyanobacterium Synechocystis sp. PCC6803, *Plant Cell Physiol.*, 2005, **46**(1), 136–146.

46 S. Masuda, K. Hasegawa and T.-A. Ono, Light-induced structural changes of apoprotein and chromophore in the sensor of blue light using FAD (BLUF) domain of AppA for a signaling state, *Biochemistry*, 2005, **44**(4), 1215–1224.

47 S. Masuda, K. Hasegawa and T.-A. Ono, Adenosine diphosphate moiety does not participate in structural changes for the signaling state in the sensor of blue-light using FAD domain of AppA, *FEBS Lett.*, 2005, **579**(20), 4329–4332.

48 S. Masuda, K. Hasegawa and T.-A. Ono, Tryptophan at position 104 is involved in transforming light signal into

changes of β-sheet structure for the signaling state in the BLUF domain of AppA, *Plant Cell Physiol.*, 2005, **46**(12), 1894–1901.

49 K. Hasegawa, S. Masuda and T.-A. Ono, Light induced structural changes of a full-length protein and its BLUF domain in YcgF (Blrp), a blue-light sensing protein that uses FAD (BLUF), *Biochemistry*, 2006, **45**(11), 3785–3793.

50 K. Okajima, Y. Fukushima, H. Suzuki, A. Kita, Y. Ochiai, M. Katayama, Y. Shibata, K. Miki, T. Noguchi and S. Itoh, Fate determination of the flavin photoreceptions in the cyanobacterial blue light receptor TePixD (Tll0078), *J. Mol. Biol.*, 2006, **363**(1), 10–18.

51 R. Takahashi, K. Okajima, H. Suzuki, H. Nakamura, M. Ikeuchi and T. Noguchi, FTIR study on the hydrogen bond structure of a key tyrosine residue in the flavin-binding blue light sensor TePixD from Thermosynechococcus elongatus, *Biochemistry*, 2007, **46**(22), 6459–6467.

52 A. Haigney, A. Lukacs, R. Brust, R.-K. Zhao, M. Towrie, G. M. Greetham, I. Clark, B. Illarionov, A. Bacher and R.-R. Kim, Vibrational assignment of the ultrafast infrared spectrum of the photoactivatable flavoprotein AppA, *J. Phys. Chem. B*, 2012, **116**(35), 10722–10729.

53 A. Haigney, A. Lukacs, R.-K. Zhao, A. L. Stelling, R. Brust, R.-R. Kim, M. Kondo, I. Clark, M. Towrie and G. M. Greetham, Ultrafast infrared spectroscopy of an isotope-labeled photoactivatable flavoprotein, *Biochemistry*, 2011, **50**(8), 1321–1328.

54 A. Lukacs, A. Haigney, R. Brust, R.-K. Zhao, A. L. Stelling, I. P. Clark, M. Towrie, G. M. Greetham, S. R. Meech and P. J. Tonge, Photoexcitation of the blue light using FAD photoreceptor AppA results in ultrafast changes to the protein matrix, *J. Am. Chem. Soc.*, 2011, **133**(42), 16893–16900.

55 T. Iwata, A. Watanabe, M. Iseki, M. Watanabe and H. Kandori, Strong donation of the hydrogen bond of tyrosine during photoactivation of the BLUF domain, *J. Phys. Chem. Lett.*, 2011, **2**(9), 1015–1019.

56 T. Kottke, A. Batschauer, M. Ahmad and J. Heberle, Blue-Light-Induced Changes in Arabidopsis Cryptochrome 1 Probed by FTIR Difference Spectroscopy, *Biochemistry*, 2006, **45**(8), 2472–2479.

57 E. Schleicher, B. Heßling, V. Illarionova, A. Bacher, S. Weber, G. Richter and K. Gerwert, Light-induced reactions of Escherichia coli DNA photolyase monitored by Fourier transform infrared spectroscopy, *FEBS J.*, 2005, **272**(8), 1855–1866.

58 T. Iwata, Y. Zhang, K. Hitomi, E. D. Getzoff and H. Kandori, Key dynamics of conserved asparagine in a cryptochrome/photolyase family protein by Fourier transform infrared spectroscopy, *Biochemistry*, 2010, **49**(41), 8882–8891.

59 D. Immeln, R. Pokorny, E. Herman, J. Moldt, A. Batschauer and T. Kottke, Photoreaction of plant and DASH cryptochromes probed by infrared spectroscopy: the neutral radical state of flavoproteins, *J. Phys. Chem. B*, 2010, **114**(51), 17155–17161.

60 I. M. M. Wijaya, Y. Zhang, T. Iwata, J. Yamamoto, K. Hitomi, S. Iwai, E. D. Getzoff and H. Kandori, Detection of distinct α-helical rearrangements of cyclobutane pyrimidine dimer photolyase upon substrate binding by Fourier transform infrared spectroscopy, *Biochemistry*, 2013, **52**(6), 1019–1027.

61 J. Zhu, T. Mathes, Y. Hontani, M. T. Alexandre, K. C. Toh, P. Hegemann and J. T. Kennis, Photoadduct Formation from the FMN Singlet Excited State in the LOV2 Domain of Chlamydomonas reinhardtii Phototropin, *J. Phys. Chem. Lett.*, 2016, **7**(21), 4380–4384.

62 J. P. Zayner, T. Mathes, T. R. Sosnick and J. T. M. Kennis, Helical Contributions Mediate Light-Activated Conformational Change in the LOV2 Domain of Avena sativa Phototropin 1, *ACS Omega*, 2019, **4**(1), 1238–1243.

63 Y. Hontani, J. Mehlhorn, T. Domratcheva, S. Beck, M. Kloz, P. Hegemann, T. Mathes and J. T. M. Kennis, Spectroscopic and Computational Observation of Glutamine Tautomerization in the Blue Light Sensing Using Flavin Domain Photoreaction, *J. Am. Chem. Soc.*, 2023, **145**(2), 1040–1052.

64 H. Kandori, Structure/Function Study of Photoreceptive Proteins by FTIR Spectroscopy, *Bull. Chem. Soc. Jpn.*, 2020, **93**(7), 904–926.

65 T. Iwata, D. Nozaki, A. Yamamoto, T. Koyama, Y. Nishina, K. Shiga, S. Tokutomi, M. Unno and H. Kandori, Hydrogen Bonding Environment of the N3-H Group of Flavin Mononucleotide in the Light Oxygen Voltage Domains of Phototropins, *Biochemistry*, 2017, **56**(24), 3099–3108.

66 T. Iwata, T. Nagai, S. Ito, S. Osoegawa, M. Iseki, M. Watanabe, M. Unno, S. Kitagawa and H. Kandori, Hydrogen Bonding Environments in the Photocycle Process around the Flavin Chromophore of the AppA-BLUF domain, *J. Am. Chem. Soc.*, 2018, **140**(38), 11982–11991.

67 T. Iwata, D. Yamada, K. Mikuni, K. Agata, K. Hitomi, E. D. Getzoff and H. Kandori, ATP binding promotes light-induced structural changes to the protein moiety of Arabidopsis cryptochrome 1, *Photochem. Photobiol. Sci.*, 2020, **19**(10), 1326–1331.

68 T. Iwata and S. Masuda, Photoreaction mechanisms of Flavoprotein photoreceptors and their applications, *Optogenetics: light-sensing proteins and their applications in Neuroscience and beyond*, 2021, pp. 189–206.

69 R. N. A. Maia, D. Ehrenberg, S. Oldemeyer, E. Kniepps-Grunhagen, U. Krauss and J. Heberle, Real-Time Tracking of Proton Transfer from the Reactive Cysteine to the Flavin Chromophore of a Photosensing Light Oxygen Voltage Protein, *J. Am. Chem. Soc.*, 2021, **143**(32), 12535–12542.

70 A. A. Gil, S. P. Laptenok, J. B. French, J. N. Iuliano, A. Lukacs, C. R. Hall, I. V. Sazanovich, G. M. Greetham, A. Bacher, B. Illarionov, M. Fischer, P. J. Tonge and S. R. Meech, Femtosecond to Millisecond Dynamics of Light Induced Allostery in the Avena sativa LOV Domain, *J. Phys. Chem. B*, 2017, **121**(5), 1010–1019.

71 L. Goett-Zink, J. L. Klocke, L. A. K. Bogeholz and T. Kottke, In-cell infrared difference spectroscopy of LOV photoreceptors reveals structural responses to light altered in living cells, *J. Biol. Chem.*, 2020, **295**(33), 11729–11741.

72 P. E. Konold, T. Mathes, J. R. Weiβenborn, M. L. Groot, P. Hegemann and J. T. Kennis, Unfolding of the C-terminal Jα helix in the LOV2 photoreceptor domain observed by time-resolved vibrational spectroscopy, *J. Phys. Chem. Lett.*, 2016, **7**(17), 3472–3476.

73 T. Fujisawa and S. Masuda, Light-induced chromophore and protein responses and mechanical signal transduction of BLUF proteins, *Biophys. Rev.*, 2018, **10**(2), 327–337.

74 S. Masuda, K. Hasegawa and T. A. Ono, Light-induced structural changes of apoprotein and chromophore in the sensor of blue light using FAD (BLUF) domain of AppA for a signaling state, *Biochemistry*, 2005, **44**(4), 1215–1224.

75 S. Masuda, K. Hasegawa, A. Ishii and T. A. Ono, Light-induced structural changes in a putative blue-light receptor with a novel FAD binding fold sensor of blue-light using FAD (BLUF); Slr1694 of synechocystis sp. PCC6803, *Biochemistry*, 2004, **43**(18), 5304–5313.

76 S. Kikuchi, M. Unno, K. Zikihara, S. Tokutomi and S. Yamauchi, Vibrational assignment of the flavin-cysteinyl adduct in a signaling state of the LOV domain in FKF1, *J. Phys. Chem. B*, 2009, **113**(9), 2913–2921.

77 M. Kondo, J. Nappa, K. L. Ronayne, A. L. Stelling, P. J. Tonge and S. R. Meech, Ultrafast Vibrational Spectroscopy of the Flavin Chromophore, *J. Phys. Chem. B*, 2006, **110**(41), 20107–20110.

78 S. P. Laptenok, A. Lukacs, R. Brust, A. Haigney, A. Gil, M. Towrie, G. M. Greetham, P. J. Tonge and S. R. Meech, Electron transfer quenching in light adapted and mutant forms of the AppA BLUF domain, *Faraday Discuss.*, 2015, **177**, 293–311.

79 A. A. Gil, A. Haigney, S. P. Laptenok, R. Brust, A. Lukacs, J. N. Iuliano, J. Jeng, E. H. Melief, R.-K. Zhao and E. Yoon, Mechanism of the AppABLUF photocycle probed by site-specific incorporation of fluorotyrosine residues: effect of the Y21 pK_a on the forward and reverse ground-state reactions, *J. Am. Chem. Soc.*, 2016, **138**(3), 926–935.

80 Y. He, A. A. Gil, S. P. Laptenok, A. Fatima, J. T. Collado, J. N. Iuliano, H. A. Woroniecka, R. Brust, A. Sabbah and M. Towrie, Enhancing Proton-Coupled Electron Transfer in Blue Light Using FAD Photoreceptor AppABLUF, *J. Am. Chem. Soc.*, 2024, **147**(1), 39–44.

81 Y. He, J. T. Collado, J. N. Iuliano, H. A. Woroniecka, C. R. Hall, A. A. Gil, S. P. Laptenok, G. M. Greetham, B. Illarionov and A. Bacher, Elucidating the Signal Transduction Mechanism of the Blue-Light-Regulated Photoreceptor YtvA: From Photoactivation to Downstream Regulation, *ACS Chem. Biol.*, 2024, **19**(3), 696–706.

82 A. Lukacs, P. J. Tonge and S. R. Meech, Photophysics of the blue light using flavin domain, *Acc. Chem. Res.*, 2022, **55**(3), 402–414.

83 K. Pirisi, L. Nag, Z. Fekete, J. N. Iuliano, J. Tolentino Collado, I. P. Clark, I. Pecsi, P. Sournia, U. Liebl, G. M. Greetham, P. J. Tonge, S. R. Meech, M. H. Vos and A. Lukacs, Identification of the vibrational marker of tyrosine cation radical using ultrafast transient infrared spectroscopy of flavoprotein systems, *Photochem. Photobiol. Sci.*, 2021, **20**(3), 369–378.

84 J. N. Iuliano, J. T. Collado, A. A. Gil, P. T. Ravindran, A. Lukacs, S. Shin, H. A. Woroniecka, K. Adamczyk, J. M. Aramini, U. R. Edupuganti, C. R. Hall, G. M. Greetham, I. V. Sazanovich, I. P. Clark, T. Daryaee, J. E. Toettcher, J. B. French, K. H. Gardner, C. L. Simmerling, S. R. Meech and P. J. Tonge, Unraveling the Mechanism of a LOV Domain Optogenetic Sensor: A Glutamine Lever Induces Unfolding of the Jalpha Helix, *ACS Chem. Biol.*, 2020, **15**(10), 2752–2765.

85 J. N. Iuliano, A. A. Gil, S. P. Laptenok, C. R. Hall, J. Tolentino Collado, A. Lukacs, S. A. Hag Ahmed, J. Abyad, T. Daryaee, G. M. Greetham, I. V. Sazanovich, B. Illarionov, A. Bacher, M. Fischer, M. Towrie, J. B. French, S. R. Meech and P. J. Tonge, Variation in LOV Photoreceptor Activation Dynamics Probed by Time-Resolved Infrared Spectroscopy, *Biochemistry*, 2018, **57**(5), 620–630.

86 A. A. Gil, S. P. Laptenok, J. N. Iuliano, A. Lukacs, A. Verma, C. R. Hall, G. E. Yoon, R. Brust, G. M. Greetham, M. Towrie, J. B. French, S. R. Meech and P. J. Tonge, Photoactivation of the BLUF Protein PixD Probed by the Site-Specific Incorporation of Fluorotyrosine Residues, *J. Am. Chem. Soc.*, 2017, **139**(41), 14638–14648.

87 M. M. N. Wolf, C. Schumann, R. Gross, T. Domratcheva and R. Diller, Ultrafast Infrared Spectroscopy of Riboflavin: Dynamics, Electronic Structure, and Vibrational Mode Analysis, *J. Phys. Chem. B*, 2008, **112**(42), 13424–13432.

88 T. Domratcheva, E. Hartmann, I. Schlichting and T. Kottke, Evidence for Tautomerisation of Glutamine in BLUF Blue Light Receptors by Vibrational Spectroscopy and Computational Chemistry, *Sci. Rep.*, 2016, **6**, 22669.

89 I. M. Wijaya, T. Domratcheva, T. Iwata, E. D. Getzoff and H. Kandori, Single Hydrogen Bond Donation from Flavin N5 to Proximal Asparagine Ensures FAD Reduction in DNA Photolyase, *J. Am. Chem. Soc.*, 2016, **138**(13), 4368–4376.

90 Y. He, M. Barone, S. R. Meech, A. Lukacs and P. J. Tonge, Light-Driven Enzyme Catalysis: Ultrafast Mechanisms and Biochemical Implications, *Biochemistry*, 2025, **64**(12), 2491–2505.

91 S. Hashem, V. Macaluso, M. Nottoli, F. Lipparini, L. Cupellini and B. Mennucci, From crystallographic data to the solution structure of photoreceptors: the case of the AppA BLUF domain, *Chem. Sci.*, 2021, **12**(40), 13331–13342.

92 V. Macaluso, S. Hashem, M. Nottoli, F. Lipparini, L. Cupellini and B. Mennucci, Ultrafast Transient Infrared Spectroscopy of Photoreceptors with Polarizable QM/MM Dynamics, *J. Phys. Chem. B*, 2021, **125**(36), 10282–10292.

93 J. J. Goings, P. Li, Q. Zhu and S. Hammes-Schiffer, Formation of an unusual glutamine tautomer in a blue light using flavin photocycle characterizes the light-adapted state, *Proc. Natl. Acad. Sci. U. S. A.*, 2020, **117**(43), 26626–26632.

94 P. C. Andrikopoulos, A. S. Chaudhari, Y. Liu, P. E. Konold, J. T. M. Kennis, B. Schneider and G. Fuertes, QM calculations predict the energetics and infrared spectra of transient glutamine isomers in LOV photoreceptors, *Phys. Chem. Chem. Phys.*, 2021, **23**(25), 13934–13950.

95 M. G. Khrenova, A. V. Nemukhin, B. L. Grigorenko, A. I. Krylov and T. M. Domratcheva, Quantum Chemistry Calculations Provide Support to the Mechanism of the Light-Induced Structural Changes in the Flavin-Binding Photoreceptor Proteins, *J. Chem. Theory Comput.*, 2010, **6**(8), 2293–2302.

96 J. M. Christie, K. Hitomi, A. S. Arvai, K. A. Hartfield, M. Mettlen, A. J. Pratt, J. A. Tainer and E. D. Getzoff, Structural tuning of the fluorescent protein iLOV for improved photostability, *J. Biol. Chem.*, 2012, **287**(26), 22295–22304.

97 J. N. Iuliano, J. B. French and P. J. Tonge, Chapter Eight – Vibrational spectroscopy of flavoproteins, in *Methods in Enzymology*, ed. B. A. Palfey, Academic Press, 2019, vol. 620, pp. 189–214.

98 M. Abe, Y. Kyogoku, T. Kitagawa, K. Kawano, N. Ohishi, A. Takai-Suzuki and K. Yagi, lnfrared spectra and molecular association of lumiflavin and riboflavin derivatives, *Spectrochim. Acta, Part A*, 1986, **42**(9), 1059–1068.

99 V. I. Birss, A. S. Hinman, C. E. McGarvey and J. Segal, In situ ftir thin-layer reflectance spectroscopy of flavin adenine dinucleotide at a mercury/gold electrode, *Electrochim. Acta*, 1994, **39**(16), 2449–2454.

100 Y. Nishina, K. Sato, C. Setoyama, H. Tamaoki, R. Miura and K. Shiga, Intramolecular and Intermolecular Perturbation on Electronic State of FAD Free in Solution and Bound to Flavoproteins: FTIR Spectroscopic Study by Using the C═O Stretching Vibrations as Probes, *J. Biochem.*, 2007, **142**(2), 265–272.

101 D. Yamada and H. Kandori, FTIR spectroscopy of flavin-binding photoreceptors, *Methods Mol. Biol.*, 2014, **1146**, 361–376.

102 M. Spexard, D. Immeln, C. Thöing and T. Kottke, Infrared spectrum and absorption coefficient of the cofactor flavin in water, *Vib. Spectrosc.*, 2011, **57**(2), 282–287.

103 B. Rieff, S. Bauer, G. Mathias and P. Tavan, IR Spectra of Flavins in Solution: DFT/MM Description of Redox Effects, *J. Phys. Chem. B*, 2011, **115**(9), 2117–2123.

104 B. Rieff, G. Mathias, S. Bauer and P. Tavan, Density Functional Theory Combined with Molecular Mechanics: The Infrared Spectra of Flavin in Solution, *Photochem. Photobiol.*, 2011, **87**(3), 511–523.

105 R. K. Kar, V. A. Borin, Y. Ding, J. Matysik and I. Schapiro, Spectroscopic Properties of Lumiflavin: A Quantum Chemical Study, *Photochem. Photobiol.*, 2019, **95**(2), 662–674.

106 M. P. Kabir, Y. Orozco-Gonzalez, G. Hastings and S. Gozem, The effect of hydrogen-bonding on flavin's infrared absorption spectrum, *Spectrochim. Acta, Part A*, 2021, **262**, 120110.

107 D. P. N. Le, G. Hastings and S. Gozem, How Aqueous Solvation Impacts the Frequencies and Intensities of Infrared Absorption Bands in Flavin: The Quest for a Suitable Solvent Model, *Molecules*, 2024, **29**(2), 520.

108 M. Huix-Rotllant, K. Schwinn and N. Ferré, Infrared spectroscopy from electrostatic embedding QM/MM: local normal mode analysis of infrared spectra of arabidopsis thaliana plant cryptochrome, *Phys. Chem. Chem. Phys.*, 2021, **23**(2), 1666–1674.

109 K. Schwinn, N. Ferré and M. Huix-Rotllant, Analytic QM/MM atomic charge derivatives avoiding the scaling of coupled perturbed equations with the MM subsystem size, *J. Chem. Phys.*, 2019, **151**(4), 041102.

110 K. Schwinn, N. Ferré and M. Huix-Rotllant, Efficient analytic second derivative of electrostatic embedding QM/MM energy: normal mode analysis of plant cryptochrome, *J. Chem. Theory Comput.*, 2020, **16**(6), 3816–3824.

111 K. Schwinn, N. Ferré and M. Huix-Rotllant, UV-visible absorption spectrum of FAD and its reduced forms embedded in a cryptochrome protein, *Phys. Chem. Chem. Phys.*, 2020, **22**(22), 12447–12455.

112 M. Huix-Rotllant and N. Ferre, Analytic Energy, Gradient, and Hessian of Electrostatic Embedding QM/MM Based on Electrostatic Potential-Fitted Atomic Charges Scaling Linearly with the MM Subsystem Size, *J. Chem. Theory Comput.*, 2021, **17**(1), 538–548.

113 M. Huix-Rotllant and N. Ferré, An Effective Procedure for Analyzing Molecular Vibrations in Terms of Local Fragment Modes, *J. Chem. Theory Comput.*, 2016, **12**(10), 4768–4777.

114 S. Dapprich, I. Komáromi, K. S. Byun, K. Morokuma and M. J. Frisch, A new ONIOM implementation in Gaussian98. Part I. The calculation of energies, gradients, vibrational frequencies and electric field derivatives, *J. Mol. Struct.: THEOCHEM*, 1999, **461**, 1–21.

115 L. W. Chung, W. M. Sameera, R. Ramozzi, A. J. Page, M. Hatanaka, G. P. Petrova, T. V. Harris, X. Li, Z. Ke, F. Liu, H. B. Li, L. Ding and K. Morokuma, The ONIOM Method and Its Applications, *Chem. Rev.*, 2015, **115**(12), 5678–5796.

116 S. J. Mo, T. Vreven, B. Mennucci, K. Morokuma and J. Tomasi, Theoretical study of the SN_2 reaction of Cl–(H_2O) + CH_3Cl using our own N-layered integrated molecular orbital and molecular mechanics polarizable continuum model method (ONIOM, PCM), *Theor. Chem. Acc.*, 2004, **111**(2), 154–161.

117 T. Vreven, B. Mennucci, C. O. da Silva, K. Morokuma and J. Tomasi, The ONIOM-PCM method: combining the hybrid molecular orbital method and the polarizable continuum model for solvation. Application to the geometry and properties of a merocyanine in solution, *J. Chem. Phys.*, 2001, **115**(1), 62–72.

118 S. Miertuš, E. Scrocco and J. Tomasi, Electrostatic interaction of a solute with a continuum. A direct utilizaion of AB initio molecular potentials for the prevision of solvent effects, *Chem. Phys.*, 1981, **55**(1), 117–129.

119 W. L. Jorgensen, J. Chandrasekhar, J. D. Madura, R. W. Impey and M. L. Klein, Comparison of simple potential functions for simulating liquid water, *J. Chem. Phys.*, 1983, **79**(2), 926–935.

120 C. I. Bayly, P. Cieplak, W. Cornell and P. A. Kollman, A well-behaved electrostatic potential based method using charge restraints for deriving atomic charges: the RESP model, *J. Phys. Chem.*, 1993, **97**(40), 10269–10280.

121 J. Wang, R. M. Wolf, J. W. Caldwell, P. A. Kollman and D. A. Case, Development and testing of a general amber force field, *J. Comput. Chem.*, 2004, **25**(9), 1157–1174.

122 A. Jakalian, D. B. Jack and C. I. Bayly, Fast, efficient generation of high-quality atomic charges. AM1-BCC

model: II. Parameterization and validation, *J. Comput. Chem.*, 2002, **23**(16), 1623–1641.

123 S. Elhajj, J. D'Ascenzi, S. O. Ajagbe, Y. Orozco-Gonzalez, M. Olivucci and S. Gozem, An automated QM/MM average protein electrostatic configuration approach for flavoproteins: APEC-F 2.0, *J. Chem. Phys.*, 2025, **163**(11), 112501.

124 A. Iyer, R. A. G. Reis, S. Gannavaram, M. Momin, A. M. Spring-Connell, Y. Orozco-Gonzalez, J. Agniswamy, D. Hamelberg, I. T. Weber, S. Gozem, S. Wang, M. W. Germann, G. Gadda and A. Single-Point, Mutation in D-Arginine Dehydrogenase Unlocks a Transient Conformational State Resulting in Altered Cofactor Reactivity, *Biochemistry*, 2021, **60**(9), 711–724.

125 B. D. Dratch, Y. Orozco-Gonzalez, G. Gadda and S. Gozem, Ionic Atmosphere Effect on the Absorption Spectrum of a Flavoprotein: A Reminder to Consider Solution Ions, *J. Phys. Chem. Lett.*, 2021, **12**(34), 8384–8396.

126 M. P. Kabir, D. Ouedraogo, Y. Orozco-Gonzalez, G. Gadda and S. Gozem, Alternative strategy for spectral tuning of flavin-binding fluorescent proteins, *J. Phys. Chem. B*, 2023, **127**(6), 1301–1311.

127 P. Ghosh, S. O. Ajagbe and S. Gozem, The Photophysical Path to the Triplet State in Light-Oxygen-Voltage (LOV) Domains, *Chemistry*, 2025, **31**(22), e202500117.

128 S. O. Ajagbe, P. Ghosh and S. Gozem, Protein electrostatics tune the photophysics of LOV1 and LOV2 domains in three organisms, *ChemRXiv*, 2025, preprint.

129 B. J. Jones, S. Elhajj, B. Haynes, S. Wang, I. O'Connor, S. Gozem and B. L. Greene, Measurement and Control of Crossed Potentials in a Flavoprotein, bioRxiv, 2025, preprint, 2025.09.13.676020.

130 N. Ferré and J. G. Ángyán, Approximate electrostatic interaction operator for QM/MM calculations, *Chem. Phys. Lett.*, 2002, **356**(3–4), 331–339.

131 M. P. Kabir, Y. Orozco-Gonzalez and S. Gozem, Electronic spectra of flavin in different redox and protonation states: a computational perspective on the effect of the electrostatic environment, *Phys. Chem. Chem. Phys.*, 2019, **21**(30), 16526–16537.

132 Y.-T. Kao, C. Saxena, T.-F. He, L. Guo, L. Wang, A. Sancar and D. Zhong, Ultrafast Dynamics of Flavins in Five Redox States, *J. Am. Chem. Soc.*, 2008, **130**(39), 13132–13139.

133 M. A. North, S. Bhattacharyya and D. G. Truhlar, Improved Density Functional Description of the Electrochemistry and Structure–Property Descriptors of Substituted Flavins, *J. Phys. Chem. B*, 2010, **114**(46), 14907–14915.

134 Y.-T. Kao, C. Tan, S.-H. Song, N. Öztürk, J. Li, L. Wang, A. Sancar and D. Zhong, Ultrafast Dynamics and Anionic Active States of the Flavin Cofactor in Cryptochrome and Photolyase, *J. Am. Chem. Soc.*, 2008, **130**(24), 7695–7701.

135 M. P. Allen and D. J. Tildesley, *Computer Simulation of Liquids*, Oxford University Press, 2017.

136 T. Darden, D. York and L. Pedersen, Particle mesh Ewald: An $N\log(N)$ method for Ewald sums in large systems, *J. Chem. Phys.*, 1993, **98**(12), 10089–10092.

137 U. Essmann, L. Perera, M. L. Berkowitz, T. Darden, H. Lee and L. G. Pedersen, A smooth particle mesh Ewald method, *J. Chem. Phys.*, 1995, **103**(19), 8577–8593.

138 R. Salomon-Ferrer, D. Case and R. Walker, An overview of the Amber biomolecular simulation package, *Wiley Interdiscip. Rev.: Comput. Mol. Sci.*, 2013, **3**, 198–210.

139 D. A. Case, T. E. Cheatham III, T. Darden, H. Gohlke, R. Luo, K. M. Merz Jr, A. Onufriev, C. Simmerling, B. Wang and R. J. Woods, The Amber biomolecular simulation programs, *J. Comput. Chem.*, 2005, **26**(16), 1668–1688.

140 W. Humphrey, A. Dalke and K. Schulten, VMD: visual molecular dynamics, *J. Mol. Graphics*, 1996, **14**(1), 33–38.

141 M. J. Frisch, G. W. Trucks, H. B. Schlegel, G. E. Scuseria, M. A. Robb, J. R. Cheeseman, G. Scalmani, V. Barone, G. A. Petersson, H. Nakatsuji, X. Li, M. Caricato, A. V. Marenich, J. Bloino, B. G. Janesko, R. Gomperts, B. Mennucci, H. P. Hratchian, J. V. Ortiz, A. F. Izmaylov, J. L. Sonnenberg, Williams, F. Ding, F. Lipparini, F. Egidi, J. Goings, B. Peng, A. Petrone, T. Henderson, D. Ranasinghe, V. G. Zakrzewski, J. Gao, N. Rega, G. Zheng, W. Liang, M. Hada, M. Ehara, K. Toyota, R. Fukuda, J. Hasegawa, M. Ishida, T. Nakajima, Y. Honda, O. Kitao, H. Nakai, T. Vreven, K. Throssell, J. A. Montgomery Jr., J. E. Peralta, F. Ogliaro, M. J. Bearpark, J. J. Heyd, E. N. Brothers, K. N. Kudin, V. N. Staroverov, T. A. Keith, R. Kobayashi, J. Normand, K. Raghavachari, A. P. Rendell, J. C. Burant, S. S. Iyengar, J. Tomasi, M. Cossi; J. M. Millam, M. Klene, C. Adamo, R. Cammi, J. W. Ochterski, R. L. Martin, K. Morokuma, O. Farkas, J. B. Foresman and D. J. Fox, *Gaussian 16 Rev. C.01*, Wallingford, CT, 2016.

142 S. Grimme, J. Antony, S. Ehrlich and H. Krieg, A consistent and accurate ab initio parametrization of density functional dispersion correction (DFT-D) for the 94 elements H-Pu, *J. Chem. Phys.*, 2010, **132**(15), 154104.

143 E. Cancès, B. Mennucci and J. Tomasi, A new integral equation formalism for the polarizable continuum model: theoretical background and applications to isotropic and anisotropic dielectrics, *J. Chem. Phys.*, 1997, **107**(8), 3032–3041.

144 R. D. Johnson III, NIST computational chemistry comparison and benchmark database. NIST Standard Reference Database Number 101: 2022.

145 J. C. Zapata Trujillo and L. K. McKemmish, Model chemistry recommendations for scaled harmonic frequency calculations: a benchmark study, *J. Phys. Chem. A*, 2023, **127**(7), 1715–1735.

146 M. H. Jamróz, Vibrational Energy Distribution Analysis (VEDA): scopes and limitations, *Spectrochim. Acta, Part A*, 2013, **114**, 220–230.

147 E. F. C. Byrd, C. D. Sherrill and M. Head-Gordon, The Theoretical Prediction of Molecular Radical Species: a Systematic Study of Equilibrium Geometries and Harmonic Vibrational Frequencies, *J. Phys. Chem. A*, 2001, **105**(42), 9736–9747.

148 C. Puzzarini, M. Biczysko and V. Barone, Accurate Harmonic/Anharmonic Vibrational Frequencies for Open-Shell Systems: Performances of the B3LYP/N07D Model for Semirigid Free Radicals Benchmarked by CCSD(T) Computations, *J. Chem. Theory Comput.*, 2010, **6**(3), 828–838.

149 S. Elhajj and S. Gozem, First and Second Reductions in an Aprotic Solvent: Comparing Computational and Experimental One-Electron Reduction Potentials for 345 Quinones, *J. Chem. Theory Comput.*, 2024, **20**(14), 6227–6240.

150 M. P. Kabir, P. Ghosh and S. Gozem, Electronic Structure Methods for Simulating Flavin's Spectroscopy and Photophysics: Comparison of Multi-reference, TD-DFT, and Single-Reference Wave Function Methods, *J. Phys. Chem. B*, 2024, **128**(31), 7545–7557.